materials

MDPI

Article

Electroconductive Composites from Polystyrene Block Copolymers and Cu–Alumina Filler

QuratulAin Nadeem [1], Tasneem Fatima [1], Pepijn Prinsen [2], Aziz ur Rehman [3], Rohama Gill [1,*], Rashid Mahmood [4] and Rafael Luque [2]

1 Department of Environmental Sciences, Fatima Jinnah Women University, Rawalpindi 46000, Pakistan; quratulainnadeem@hotmail.com (Q.N.); tasnem009@gmail.com (T.F.)
2 Departamento de Universidad de Córdoba, Edificio Marie Curie, Ctra Nnal IV-A, Km396, E14014 Córdoba, Spain; pepijnprinsen33@hotmail.com (P.P.); q62alsor@uco.es (R.L.)
3 Department of Chemistry, the Islamia University of Bahawalpur, Bahawalpur 63000, Pakistan; draziz@iub.edu.pk
4 Department of Chemistry, University of Azad Jammu and Kashmir Chehla Campus Muzaffarabad, Muzaffarabad 13100, Pakistan; rashid_meh786@yahoo.com
* Correspondence: rohama_gill@hotmail.com or rohamag@gmail.com; Tel.: +92-51-9292-900 (ext. 101)

Academic Editor: Reza Montazami
Received: 20 October 2016; Accepted: 1 December 2016; Published: 7 December 2016

Abstract: Technological advancements and development of new materials may lead to the manufacture of sustainable energy-conducting devices used in the energy sector. This research attempts to fabricate novel electroconductive and mechanically stable nanocomposites via an electroless deposition (ELD) technique using electrically insulating materials. Metallic Cu is coated onto Al_2O_3 by ELD, and the prepared filler is then integrated (2–14 wt %) into a matrix of polystyrene-block-poly(ethylene-ran-butylene)-block-polystyrene-graft-maleic anhydride (PS-*b*-(PE-*r*-B)-*b*-PS-*g*-MA). Considerable variations in composite phases with filler inclusion exist. The Cu crystallite growth onto Al_2O_3 was evaluated by X-ray diffraction (XRD) analysis and energy dispersive spectrometry (EDS). Scanning electron microscopy (SEM) depicts a uniform Cu coating on Al_2O_3, while homogeneous filler dispersion is exhibited in the case of composites. The electrical behavior of composites is enhanced drastically (7.7×10^{-5} S/cm) upon incorporation of Cu–Al_2O_3 into an insulating polymer matrix (4.4×10^{-16} S/cm). Moreover, mechanical (Young's modulus, tensile strength and % elongation at break) and thermal (thermogravimetric analysis (TGA), derivative thermogravimetry (DTG), and differential scanning calorimetry (DSC)) properties of the nanocomposites also improve substantially. These composites are likely to meet the demands of modern high-strength electroconductive devices.

Keywords: copolymers; composites; morphology; mechanical properties; thermal properties

1. Introduction

Technological advances highly depend on the development of a wide diversity of new materials. Conductive polymer composites (CPCs) have an array of applications in various industries, among them the electronic industry, which made revolutionary developments both in manufacturing and recycling. Electrostatic discharge (ESD) and electromagnetic interference (EMI) are phenomena that affect the economy of the electronic industry. They can arise during manufacturing, packing, conveyance, and working. Thus, the use of appropriate EMI-shielding materials to reduce electric energy losses is essential [1]. The ever-growing electronic waste (e-waste) is now posing devastating impact on the environment due to its accumulation. One way to reduce this accumulation is to increase the life span of electronics to protect them from the detrimental effects of EMI and ESD. Design and

application of CPCs as advanced materials have been shown to expand the shelf life of electronics, which may ultimately reduce the production of e-waste [2]. Although, production of various classes of conducting polymer nanocomposites on a commercial scale is growing at a rapid pace, yet metal-filled CPCs exhibit poor mechanical properties and are no longer preferred by modern industries due to their high cost. To provide exceptional electrical properties without compromising the mechanical behavior, researchers switched their focus towards metal-coating techniques such as electrodeposition, chemical vapor deposition, physical vapor deposition, electrospinning, and others. Among them, electroless deposition (ELD) is a novel metal deposition technique. The ELD-plating technique is able to incorporate desired properties of a metallic coating irrespective of the substrate geometry and at low temperature. This coating technique is redox-sensitive, as the internal current is supplied by the oxidation of a reducing agent [3,4], thus uniform plating can also be carried out inside the holes, recesses, and non-line-of-sight surfaces [5–7]. A variety of metals—such as Ag, Cu, Au, and Ni (in order of decreasing conductivity)—have been coated on different substrates via ELD to fabricate electrically conductive materials like conductive plates, wires, rods, and powders for various electronic applications [8–10].

The novelty of the present research work lies in the preparation of electrically conductive Cu-coated alumina powder via ELD, which was then used, for the first time, as filler in a matrix of polystyrene-block-poly(ethylene-ran-butylene)-block-polystyrene-graft-maleic anhydride (PS-*b*-(PE-*r*-B)-*b*-PS-*g*-MA). The selected polymer matrix is electrically insulating and offers the characteristics of vulcanized rubber without going through the process of vulcanization. Also, the presence of styrene maleic anhydride (SMA) segments in the copolymer elevates the glass transition temperature (T_g). The appropriate interfacial properties of the matrix [11,12] makes it suitable for the preparation of blends and composites. The limitations of the selected copolymer are its low strength and stiffness [13]. Alumina is used in numerous applications in various fields due to its excellent mechanical properties, anticorrosivity, wear resistance, and hardness. The presence of Cu in the ELD-deposited metal-ceramic filler enhances the electrical conductivity and the incorporation of Al_2O_3 increases the mechanical strength, compensating for the low strength and stiffness of the copolymer. The resultant concoction may improve the durability of advanced material applications, such as EMI- and ESD-shielding materials [8], heat sinks for microelectronics [14], sensors for biomedical usage [9], and so on.

2. Experimental Section

This research work focused on the synthesis and characterization of conductive composites by adding a conductive ceramic filler, coated with a metal through ELD technique, in a nonconducting polymer.

2.1. Materials

The following analytical-grade chemicals were used: Fluka Chemika (Buchs, Switzerland, aluminium oxide (Al_2O_3)), Riedel-de Haen (Seelze, Germany, nitric acid (HNO_3 37%), copper sulphate pentahydrate ($CuSO_4 \cdot 5H_2O$), and potassium sodium tartrate ($KNaC_4H_4O_6 \cdot 4H_2O$)), Merck (Darmstadt, Germany, hydrofluoric acid (HF)), Scharlau (Barcelona, Spain, sodium hydroxide (NaOH)), Sigma Aldrich (Buchs, Switzerland, polyethylene glycol ($C_{2n}H_{4n+2}O_{n+1}$), thiourea (CH_4N_2S), palladium chloride ($PdCl_2$), stannous chloride ($SnCl_2 \cdot 2H_2O$), ethylenediaminetetraacetic acid disodium salt ($C_{10}H_{14}N_2Na_2O_8$), formaldehyde solution (HCHO), dimethylamine borane ($C_4H_{10}BN$), boric acid (H_3BO_3), chloroform ($CHCl_3$), and polystyrene-block-poly(ethylene-ran-butylene)-block-polystyrene-graft-maleic anhydride (PS-*b*-(PE-*r*-B)-*b*-PS-*g*-MA)).

2.2. Preparation of Conductive Filler

Electroless deposition (ELD) method was employed for the preparation of conductive filler. Copper (Cu) deposition onto Al_2O_3 substrate was accomplished after successive substrate pretreatment steps.

2.2.1. Pretreatment of Al_2O_3

Pretreatment of Al_2O_3 was done before the deposition step, followed by surface cleaning and surface activation. To avoid tedious filtration steps, Al_2O_3 was packed in commercially available silk cloth (160 mesh) and was dipped in subsequent solutions rather than dispersion in solution, which may also increase the reaction time. First, the Al_2O_3 substrate was dipped in concentrated HNO_3 (2 min) to remove oil and dirt. Acid-cleaned Al_2O_3 was dipped in catalytic activator solution containing 0.03 mmol of $PdCl_2$ and 0.246 mmol of $SnCl_2$ in 40 mL of concentrated HCl (14 min). After activation, the substrate was introduced to a reduction bath made of 4.74 mmol of ($C_4H_{10}BN$) and 4.52 mmol of (H_3BO_3) in a sufficient quantity of distilled water (7 min). Each step of pretreatment was followed by 1 min rinsing in distilled water. Pretreated Al_2O_3 was then used for ELD of Cu.

2.2.2. Cu Coating on Pretreated Al_2O_3

Pretreated Al_2O_3 was dipped in an electroless plating bath (Table 1). After deposition, Cu-deposited Al_2O_3 was rinsed with distilled water and oven-dried for 3–4 h at 40 °C. The prepared Cu–Al_2O_3 powder was used further as conductive filler for insulating polymer matrix.

Table 1. Composition of electroless (EL) bath and conditions used for Cu plating.

Constituents of EL Bath	Chemicals	Amount (mmol)
Metal Salt	$CuSO_4 \cdot 5H_2O$	64
Complexing Agent	$KNaC_4H_4O_6 \cdot 4H_2O$	106
	Na_2EDTA	54
	NaOH	350
Reducing Agent	HCHO	170
Stabilizer	CH_4N_2S	0.013
	$C_{2n}H_{4n+2}O_{n+1}$	50 mL
Conditions in EL bath	Temperature	45–50 °C
	Time	30 min
	pH	12.0–12.5

2.3. Synthesis of Conductive Composites

Conductive polymer composites (CPCs) were prepared by incorporating Cu–Al_2O_3 filler with varied content (2, 4, 6, 8, 10, 12, and 14 wt %) in PS-*b*-(PE-*r*-B)-*b*-PS-*g*-MA polymer matrix. PS-*b*-(PE-*r*-B)-*b*-PS-*g*-MA was dissolved in 30 mL chloroform followed by addition of the filler. The polymer–filler solution was stirred for 1–2 h at 750 rpm, poured into a Petri dish for film casting, and then detached from the mold after solvent evaporation. The prepared composite films were utilized for characterization. To attain accuracy in performance and results, samples were prepared in triplicates and the mean values were reported after characterization.

2.4. Instrumentation and Characterization

2.4.1. X-ray Diffraction (XRD) Analysis

PANalytical X-ray diffractometer (XPERT-PRO) (Düsseldorf, Germany) was used for XRD analysis of pristine Al_2O_3, Cu–Al_2O_3, PS-*b*-(PE-*r*-B)-*b*-PS-*g*-MA, and Cu–Al_2O_3/PS-*b*-(PE-*r*-B)-*b*-PS-*g*-MA composites. As Cu is the anodic material, X-rays of wavelength 1.540598 Å (Cu-Kα) were used for analysis. The 2θ data were analyzed with 0.05° scan step size, scan range 5°–70° (1 s) at 40 kV voltage and 30 mA beam current. The *d*-spacing and average crystallite size of Cu and Cu–Al_2O_3 particles were calculated by Bragg's and Scherrer's equation, respectively.

2.4.2. Morphological Analysis

The surface morphologies of pristine Al_2O_3, Cu-coated Al_2O_3, host polymer, and its respective composites were analyzed with SEM, obtained by a HT-Phys-UAJK microscope equipped with a secondary electron (SE) detector at 25 kV accelerating voltage. Fractured surfaces of composites were also examined by MIRA3 TESCAN (Nova 400 Nano, Salem, OR, USA) (SE detector at an accelerating voltage of 10 kV) to analyze the dispersion of filler in polymer matrix.

2.4.3. Energy Dispersive Spectrometry (EDS) Analysis

Elemental composition and atomic weight % of Cu coated Al_2O_3, host polymer and its respective composites were investigated by using a JSM6490LV (JEOL) microscope (Tokyo, Japan). The instrument was equipped with QUANTAX EDS XFlash detector 4010-Bruker (Billerica, MA, USA) at an accelerating voltage of 20 kV.

2.4.4. Analysis of Surface/Volume Resistivity and Electrical Conductivity

The surface resistivity ($\Omega/\square$) and volume resistivity (Ω·cm) of composites were measured by the 4-probe method using a high-resistance meter by applying the ASTM D-257 test method [15] at room temperature. A 500 V direct current field was applied through electrodes made up of tungsten carbide. Since electrical conductivity is inversely proportional to volume resistivity, electrical conductivities (S/cm) were calculated as the inverse of the volume resistivities (Ω·cm).

2.4.5. Analysis of Mechanical Properties

The mechanical features of composites were examined by calculating the Young's modulus (MPa), tensile strength (MPa), and % elongation at break according to the ASTM D638-02 [16] and ASTM D638-03 [17] test procedures for mechanical analysis. An Instron tester (4465UK, Norwood, MA, USA) was used at 20 ± 2 °C by subjecting samples with dimensions of 0.8–1.0 mm thickness and 6 mm× 70 mm (width × gauze length).

2.4.6. Analysis of Thermal Properties

Thermogravimetric analysis (TGA) was carried out with a Perkin Elmer TGA-7 (Waltham, MA, USA) in the 50–550 °C temperature range at 20 °C/min in dynamic atmosphere (20 mL/min N_2 flow) using a 2 mg sample. Non-isothermal conditions were used for recording thermal analytical results. A DSC 404-NETZSCH instrument was used for differential scanning calorimetry (DSC) analysis in the 20–500 °C range at 20 °C/min.

3. Results and Discussion

3.1. XRD Analysis of Pristine and Cu-Coated Al_2O_3 Powder and Composite Films

The prepared filler was analyzed with XRD for the determination of phase change and particle size. Scherrer's equation is used to calculate the particle size of pristine and Cu-coated Al_2O_3 as expressed in Equation (1) [18]:

$$D = \frac{K\lambda}{\beta\, cos\theta} \quad (1)$$

where D = crystallite size (nm); λ = wavelength; K = Scherrer's constant; β = angular width (radians); and θ = Bragg's angle.

Interplanar spacing between atoms within the crystallite structure is denoted by d-spacing. Bragg's equation used for the determination of d-spacing of pristine and Cu-coated Al_2O_3 is given in Equation (2).

$$2dsin\theta \;=\; n\,\lambda\;(n-1) \quad (2)$$

The XRD spectrum of pristine Al_2O_3 powder is presented in Figure 1. The three peaks at 13.13°, 46.04°, and 67.28° (2θ values), correspond to the Al_2O_3 phase. The strongest diffraction peak is observed at 67.28° with minimum *d*-spacing 0.139 nm. At 46.04°, another peak exists corresponding to Al_2O_3 with *d*-spacing 0.197 nm. The average size of the cubic lattice of Al_2O_3 is approximately 8.8 nm.

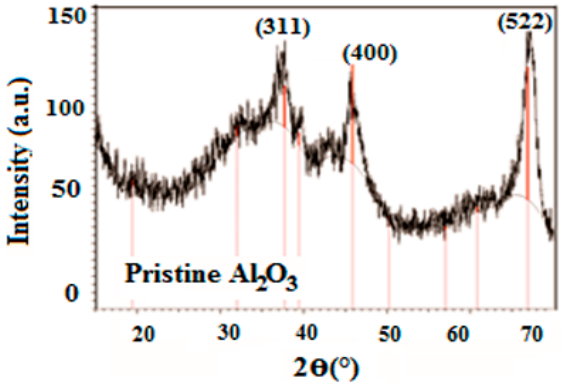

Figure 1. X-ray diffraction (XRD) pattern of pristine Al_2O_3 nanopowder.

The XRD spectrum of Cu–Al_2O_3 (Figure 2) depicts the strongest peak at 43.5° and a relatively less intense peak at 50.6° corresponding to the (111) and (200) lattice planes of Cu, respectively. The strongest diffraction peak at 43.5° is characteristic of a face-centered cubic structure with *d*-spacing of 0.21 nm; this confirms deposition of crystal-structured metallic Cu on the substrate [18,19]. The relative peak intensity at 2θ = 67.3° clearly represents the XRD pattern of pristine Al_2O_3 (Figure 1), whose amount was lower in the composite material. The disturbance observed in the peak corresponding to the Al_2O_3 phase is due to the change in the nature of original Al_2O_3 after the deposition of Cu. The average crystallite size of Cu–Al_2O_3 was calculated as approximately 26.2 nm. XRD analysis also revealed that average crystallite size of Al_2O_3 increased from 8.8 nm to 26.2 nm, which confirms the deposition of Cu crystallites, with an increase in the mean thickness to ~17.4 nm. A similar XRD pattern was reported in literature [20,21], where the strongest peak of electroless deposited-Cu appeared at 2θ = 43°.

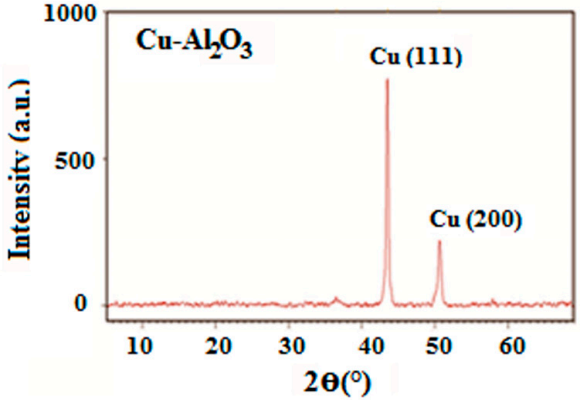

Figure 2. XRD pattern of Cu-coated Al_2O_3 nanopowder.

For determining the effect of Cu–Al_2O_3 filler in the host polymer matrix, XRD spectra of the polymer with 2 wt % and 14 wt % of Cu–Al_2O_3-loading were recorded (Figure 3). The XRD pattern of neat PS-*b*-(PE-*r*-B)-*b*-PS-*g*-MA shows a broad peak at 10°–27° and one relatively less intense peak at 48.9°, which confirms its amorphous structure. Upon 2 wt % Cu–Al_2O_3 loading in PS-*b*-(PE-*r*-B)-*b*-PS-*g*-MA, two peaks at 42.6° and 49.9° are observed. The peak at 42.6° is attributed

to the crystalline nature of Cu, while another peak at 49.9° might represent a slight peak shift from 48.92° corresponding to amorphous phase of the polymer. At 14 wt % Cu-Al_2O_3 loading, three peaks at 2θ = 36.2°, 42.9° and 50.1° arise. The sharp peak observed at 42.9° is characteristic of metallic Cu inclusion supported by another peak at 50.1° and thus confirms the crystalline phase of the prepared composites.

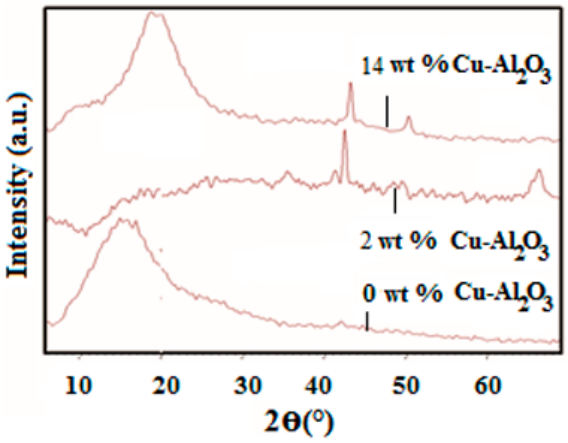

Figure 3. XRD patterns of neat polystyrene-block-poly(ethylene-ran-butylene)-block-polystyrene-graft-maleic anhydride (PS-*b*-(PE-*r*-B)-*b*-PS-*g*-MA) (0 wt % Cu-Al_2O_3) and composites with 2 wt % and 14 wt % Cu–Al_2O_3.

3.2. Morphological Study of Cu–Al_2O_3 Filler and Block Copolymer Composites

SEM analysis was used to determine the surface morphology and crystalline structure of the materials. An SEM micrograph of pristine Al_2O_3 and Cu–Al_2O_3 powder are shown in Figure 4a,b, respectively, showing a uniform Cu coating on the alumina surface. The dispersion of the filler is improved as compared to pristine alumina powder. The Cu-coated Al_2O_3 particles exhibit fine-scale roughness, characteristic of metal coating [22,23]. Silvain and co-workers also deposited Cu onto submicron-sized Al_2O_3 particles [24]. Their work revealed uniform and fine coating of metallic Cu and increased average particle size of Al_2O_3 particles after Cu deposition. The SEM image of Cu–Al_2O_3 from Wang and co-workers [25] showed good similarity (Figure 4c). In comparison, Krupa and co-workers deposited Ag on polyimide particles (Figure 4d) [26]. In all these cases, the ELD-plating technique was used. The morphological properties looked similar and seem to be rather irrespective of the type of substrate.

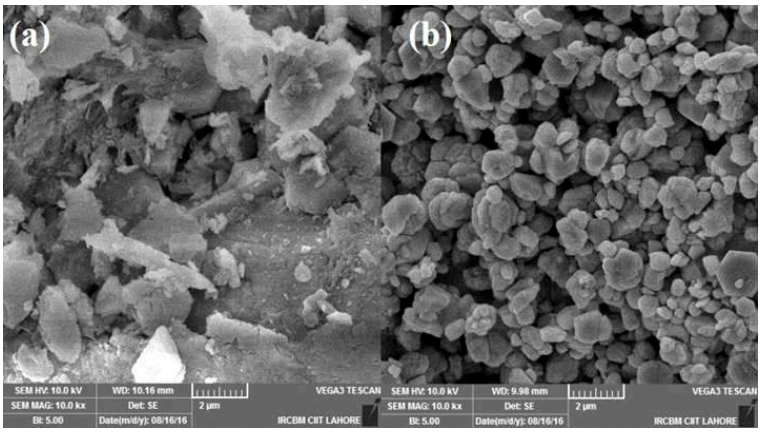

Figure 4. *Cont.*

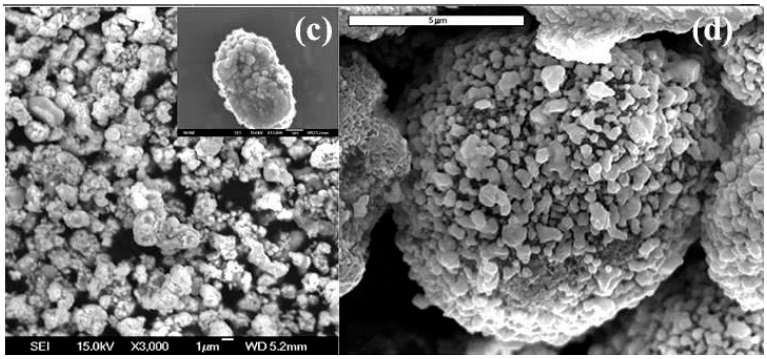

Figure 4. SEM micrographs of (**a**) pristine Al_2O_3 powder and Cu-coated Al_2O_3 (**b**) in this work; (**c**) in Wang et al. [25]; and (**d**) Ag coated onto polyimide [26].

The surface morphology of the host polymer PS-*b*-(PE-*r*-B)-*b*-PS-*g*-MA and the composite films with 2, 6, 10, and 14 wt % of Cu–Al_2O_3 are shown in Figure 5a–d. The incorporation of filler played a remarkable role on the morphology of the resultant composites. With the incorporation of lowest filler content (2 wt %), homogenous dispersion of filler is observed in both the composites predicting good filler–polymer interaction. At least 10 wt % filler is required to observe the initiation of particle-to-particle connectivities, which improve throughout the matrix when the filler content is further increased to 14 wt %. The comparison of Figure 5b,e illustrates the decreased interparticle distance. The shiny small areas in the SEM images resemble the presence of the metal coated on ceramic filler. Even smaller interparticle distance could be achieved with filler loadings higher than 14 wt %, but this compromises the mechanical performance considering the properties of ceramics. A clear transition in the particle shape and surface roughness takes place upon Cu metallization. The uniform growth of Cu crystallites on Al_2O_3 explains the change in morphology regarding particle distribution, which ultimately affects the mean coating thickness. At higher filler loading, agglomerates or islands of the filler particles are formed within the matrix material, which helps the smooth transfer of electrons. Individual nanosized filler particles are not distinctly visible in SEM micrographs because of this phenomenon [27].

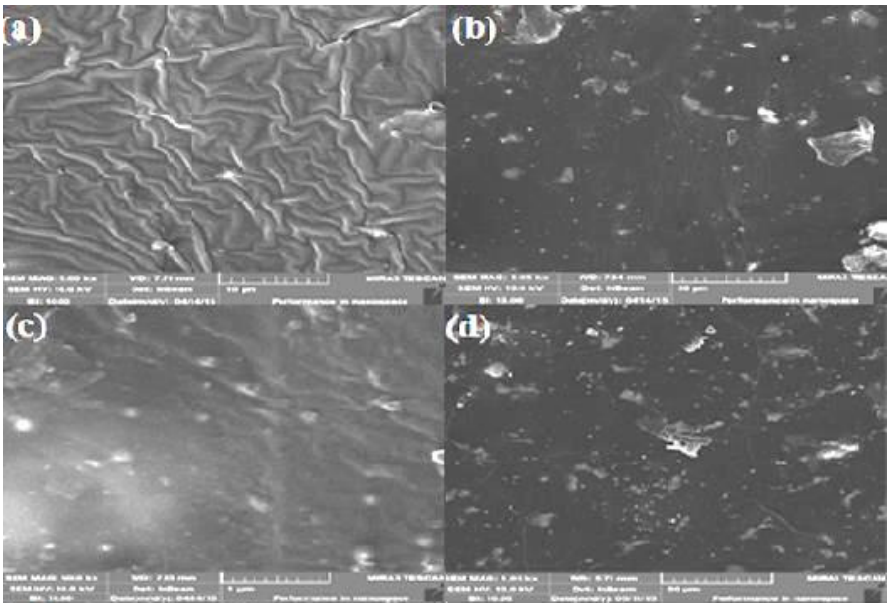

Figure 5. *Cont.*

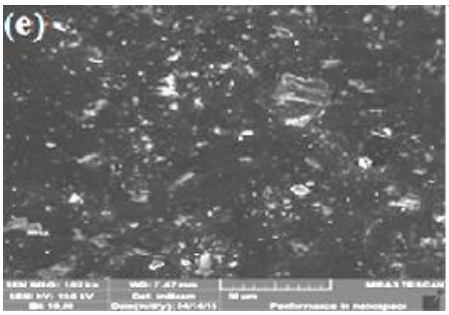

Figure 5. SEM micrographs of (**a**) PS-*b*-(PE-*r*-B)-*b*-PS-*g*-MA and composites with (**b**) 2; (**c**) 6; (**d**) 10; and (**e**) 14 wt % Cu–Al_2O_3.

3.3. EDS Analysis of Cu–Al_2O_3 Filler and Block Copolymer Composites

EDS was used to study the elemental composition of Cu–Al_2O_3 filler and Cu–Al_2O_3/PS-*b*-(PE-*r*-B)-*b*-PS-*g*-MA composites (Table 2). Cu, Al, and Pd were detected in the filler material. The high content of Cu (67.7%) followed by Al (30.4%) and Pd (1.9%) confirms the effective deposition of Cu–Al_2O_3 via the ELD process. Pd was present in small quantities, as it was used at a minor concentration for surface activation of the Al_2O_3 substrate.

Table 2. Elemental composition of Cu–Al_2O_3/PS-*b*-(PE-*r*-B)-*b*-PS-*g*-MA composites.

Cu–Al_2O_3 (wt %)	Atomic wt % of Elements			
	C	O	Al	Cu
0	95.3	4.7	–	–
2	85.1	4.3	1.3	9.3
14	79.2	3.5	0.4	16.9

3.4. Surface/Volume Resistivity and Electrical Conductivity of Block Copolymer Composites

The volume resistivity is the reciprocal of the electric conductivity. Measurement of the resistance across the materials' surface, which is in contact with the electrodes, is termed surface resistivity (Ω/sq or Ω/□) [28,29], while electrical resistance through a cube of insulating material is considered as volume resistivity (Ω·cm). The host matrix polymers are usually non-conducting in nature and contain an insignificant number of charge carriers in free-state. Thus, the electrical properties of such matrix polymer composites almost exclusively depend on the selection of filler and its ability to form smooth conductive networks throughout the matrix [30–35]. The surface resistivity of Cu–Al_2O_3/PS-*b*-(PE-*r*-B)-*b*-PS-*g*-MA matrix composites with increasing filler loadings (2–14 wt %) were studied. The surface and volume resistivity of neat polymer was also analyzed to determine its electrical behavior as intrinsic or extrinsic conducting polymer matrix. Table 3 shows the surface resistivity, the volume resistivity, and the electrical conductivity. The values for PS-*b*-(PE-*r*-B)-*b*-PS-*g*-MA are 2.30×10^{14} Ω/□, 2.3×10^{15} Ω·cm, and 4.348×10^{-16} S/cm, respectively, which confirms that it cannot act as intrinsic conducting polymer; although bulky aromatic rings are present as pendants, the main chain is saturated, rendering an insulation material.

With the inclusion of small amounts of filler (2 wt %), the surface resistivity of the corresponding composite readily drops from insulating to antistatic region. The corresponding electrical conductivity increases to 2.381×10^{14} Ω·cm. This immediate shift from insulating to antistatic region might be attributed to the connection with unsaturated side chain substitutions like maleic anhydride and benzene groups, which essentially help to enhance particle-to-particle interaction [36]. By increasing the loading of Cu–Al_2O_3 filler in the polymer matrix from 4 to 12 wt %, the surface and volume resistivity drop from 5.8×10^9 to 1.3×10^8 Ω/□ and from 4.2×10^{13} to 4.5×10^4 Ω·cm, respectively. This drop shifts the conductive properties of the material from the antistatic to the static dissipative

region [37]. Upon further incorporation of filler (14 wt %), the surface resistivity drops drastically to 4.0×10^4 Ω/□, while the volume resistivity and electric conductivity changed only substantially compared to 12 wt % filler loading. The gradual increment in conductivity with addition of 2–14 wt % filler is shown in Figure 6. It confirms network formation as suggested by the SEM results, showing the transition from an insulating to a semiconducting region.

Table 3. Surface/volume resistivity and electrical conductivity of Cu–Al_2O_3/PS-*b*-(PE-*r*-B)-*b*-PS-*g*-MA composites.

Cu–Al_2O_3 (wt %)	Surface Resistivity (Ω/□)	Volume Resistivity (Ω·cm)	Electrical Conductivity (S/cm)
0	2.3×10^{14}	2.3×10^{15}	4.35×10^{-16}
2	4.2×10^{10}	4.2×10^{13}	2.38×10^{-14}
4	5.8×10^{9}	5.8×10^{12}	1.72×10^{-13}
6	5.1×10^{9}	5.1×10^{10}	1.96×10^{-11}
8	2.3×10^{8}	2.3×10^{7}	4.35×10^{-8}
10	2.1×10^{8}	2.1×10^{6}	4.76×10^{-7}
12	1.3×10^{8}	4.5×10^{4}	2.22×10^{-5}
14	4.0×10^{4}	1.3×10^{4}	7.69×10^{-5}

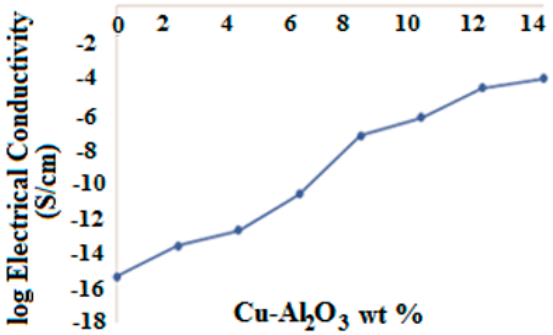

Figure 6. Electrical conductivity of Cu–Al_2O_3/PS-*b*-(PE-*r*-B)-*b*-PS-*g*-MA composites.

The electron transfer responsible for conductivity throughout the Cu–Al_2O_3/PS-*b*-(PE-*r*-B)-*b*-PS-*g*-MA matrix takes place when interaction zones between filler and matrix find connections (Figure 7), establishing a web [38–41]. Cu–Al_2O_3/PS-*b*-(PE-*r*-B)-*b*-PS-*g*-MA composites are cost-effective materials, as they showed enhanced electrical conductivity and they are easy to prepare compared to previously cited literature [42]. Beyond the critical concentration or percolation limit, there is no further significant increase in electrical conductivity even though more filler is contained in the composite material. Once the saturation point is attained, further increase in filler loading may only increase the sum of conductive networks and does not contribute in further conductivity increments. In contrast, shielding effectiveness may increase when higher filler loadings are used [43–45].

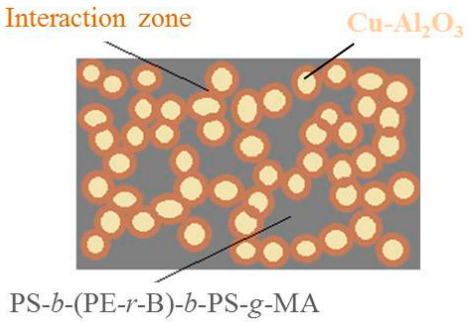

Figure 7. Schematic illustration of interaction between Cu–Al_2O_3 conductive filler and PS-*b*-(PE-*r*-B)-*b*-PS-*g*-MA polymer matrix responsible for electron transfer.

3.5. Mechanical Properties of Cu–Al_2O_3/PS-b-(PE-r-B)-b-PS-g-MA Composites

Mechanical performance of a polymer matrix composite can be influenced by the composition and interaction of filler and matrix materials used. Geometrical aspects, such as structure shape and size of reinforcement material, considerably affect the mechanical behavior of composites [46]. For the synthesis of structurally resilient composites, filler dispersion and declustering is a prerequisite. Thus, by critically controlling the volume fraction of filler, mechanical properties were measured to analyze the effect of filler inclusion and to prevent any deterioration in mechanical properties of composites [45]. The mechanical behavior of Cu–Al_2O_3/polymer composites was examined by calculating Young's modulus, tensile strength, and % elongation at break of the composites with increasing filler loading (0–14 wt %).

3.5.1. Young's Modulus

Young's modulus is a quantitative parameter for the stiffness determination of elastic materials. It is defined as the ratio of applied stress to the strain along the same axis. The applied stress should be in the range in which Hook's law holds properly [47]. Young's modulus of neat block copolymer is 50 ± 3 MPa, which increased to 150 ± 3 MPa (Figure 8) with the gradual addition of reinforcement material. This gradual and constant increase in Young's modulus of composites with increased filler loading indicates enhancement in stiffness imparted by Al_2O_3.

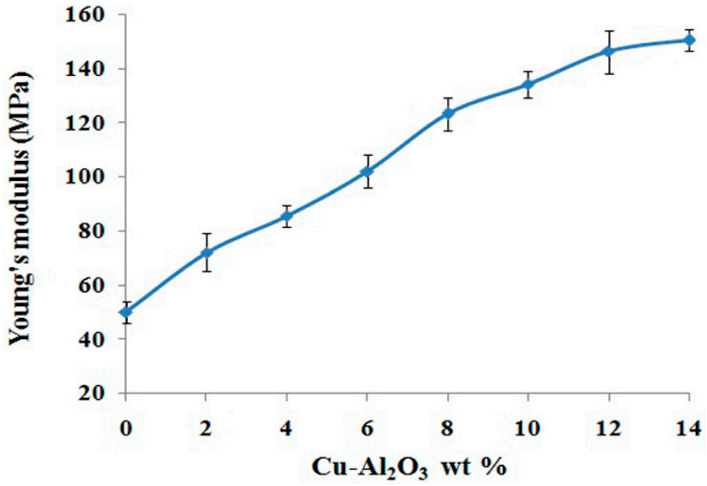

Figure 8. Young's modulus of Cu–Al_2O_3/PS-*b*-(PE-*r*-B)-*b*-PS-*g*-MA composites.

3.5.2. Tensile Strength

The maximum stress that a material can endure before failing or breaking is known as tensile strength [48]. The incorporation of Cu–Al_2O_3 in the polymer matrix increases the tensile strength of the resultant composites. At 14 wt % Cu–Al_2O_3 loading, the tensile strength of the composite reached 82 ± 3 MPa, as compared to 15 ± 3 MPa of the neat polymer. Figure 9 shows the gradual increase of tensile strength with filler loading. Tensile strength is strongly dependent upon interfacial adhesion/bonding between filler and matrix and is aided by uniform filler dispersion. Interfacial adhesion determines the strength of such composites. The results suggest good compatibility between particulate filler and polymer matrix and confirms active transfer of stress from matrix to particulate filler [49–51]. The PS-*b*-(PE-*r*-B)-*b*-PS-*g*-MA/Cu-Al_2O_3 composites offer good strength and mechanical resistance, compared to previously reported polymer/metal-coated polymers [26], polymer/carbon [42], polymer/ceramic [52], polymer/mineral ([53,54], ethylene–propylene–diene monomer rubber/$Mg(OH)_2$) [55] and polymer/polymer composites [53], as illustrated in Table 4.

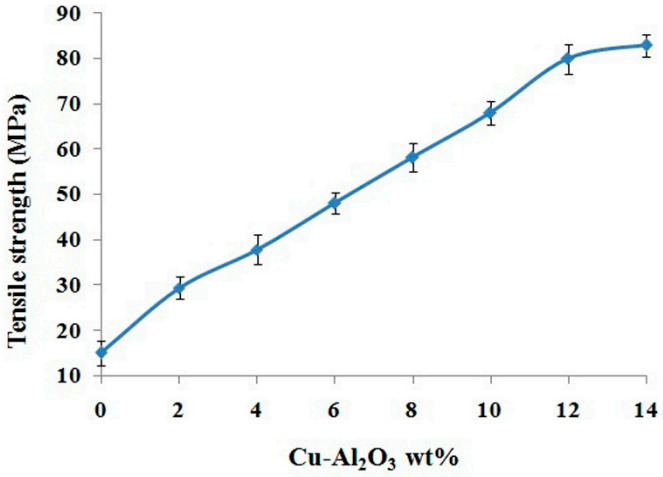

Figure 9. Tensile strength of Cu–Al_2O_3/PS-*b*-(PE-*r*-B)-*b*-PS-*g*-MA composites.

Table 4. Comparison of the tensile strength of PS-*b*-(PE-*r*-B)-*b*-PS-*g*-MA/Cu-Al_2O_3 composites with previously reported data.

Composite Type	Tensile Strength (MPa)	Reference
PS-*b*-(PE-*r*-B)-*b*-PS-*g*-MA/Cu-Al_2O_3	82.9	Present research
Polyethylene/Ag-coated polyamide	2.7	[26]
Waterborne polyurethane/graphene	9.6	[42]
Polyurethane/silica	6.80	[52]
Polypropylene/$CaCO_3$	29.7	[53]
Polypropylene/$BaSO_4$	30.0	[54]
Ethylene–propylene–diene monomer rubber/$MgOH_2$	9.6	[55]
Polypropylene/poly(methylmethacrylate)	29.5	[53]

3.5.3. Elongation at Break

Elongation at break is a quantitative parameter for the ductility of the material. It is defined as the percentage of elongation of a material from zero stress to the breaking point of that material [56]. The elongation at break is also an indicator for determining the toughness of two phase materials [57]. The elongation at break calculated for PS-*b*-(PE-*r*-B)-*b*-PS-*g*-MA polymer was 16.9% ± 0.4%. Cu–Al_2O_3/PS-*b*-(PE-*r*-B)-*b*-PS-*g*-MA composites with increasing filler loadings (0%–14%) showed a gradual decrease from 16.9% to 10.1% (Figure 10). Polymers are ductile in nature while ceramics exhibit brittle behavior. Thus, the gradual increase in brittle behavior is due to the incorporation of the reinforcement material [58], and may arise from interstructural progression in which filler particles are dispersed in the interaggregate space [48]. At low filler loading, the matrix is not adequately reinforced. So, it could not withstand high load, and eventually failure happens at lower elongation. However, at higher filler loading, the matrix is increasingly reinforced and endures high load before the breaking point is reached. The reinforcement mechanism preludes that, at higher filler loading, the molecular mobility drops because of the formation of physical bonds among particles of filler and polymer molecule chains [43].

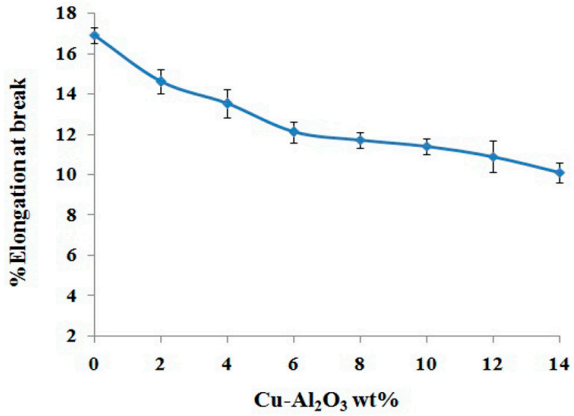

Figure 10. Elongation at break of Cu–Al_2O_3/PS-*b*-(PE-*r*-B)-*b*-PS-*g*-MA composites.

3.6. Thermal Characteristics of Block Copolymer Composites

3.6.1. Thermogravimetric Analysis (TGA)

TGA examines the thermal properties as the weight alteration upon heating during the phases of thermal breakdown. The thermal behavior determines the possible specific application fields of nanocomposites [59]. TGA thermograms of neat PS-*b*-(PE-*r*-B)-*b*-PS-*g*-MA and Cu–Al_2O_3 loaded composites from 0, 2, and 14 wt % are shown in Figure 11. A two-phase decomposition is observed for neat block copolymer. A slight dip at 250 °C indicates the presence of some residual low molecular weight compounds in the polymer. In the present conditions, the polymer remains stable up to 397 °C (8% weight loss). The second phase of decomposition starts at 397 °C (T_{max}) and continues up to a final degradation temperature of 480 °C (99% weight loss at T_f). With the inclusion of 2 wt % Cu–Al_2O_3, the thermal stability of the composite is improved, where T_{max} raises from 397 to 405 °C and T_f from 480 to 492 °C. At 14 wt % filler loading, T_{max} and T_f are respectively 30 °C and 9 °C higher compared to the neat polymer. At this point (T_f 489 °C), 67% residue is still left. Upon heating the polymer, the long chains break down into small fragments which might have interacted with Cu–Al_2O_3 particles and got trapped into filler particles difficult to be decomposed further, thus improving the thermal stability of the PS-*b*-(PE-*r*-B)-*b*-PS-*g*-MA composites [56]. Similar behavior was observed previously, where thermal stability was enhanced due to filler incorporation which hindered the segmental movement of polymer when intermingled with small chains of the host polymer [27,48]. Analogous degradation patterns are seen in the derivative thermogravimetry (DTG) curves of host polymer and its composites (Figure 12).

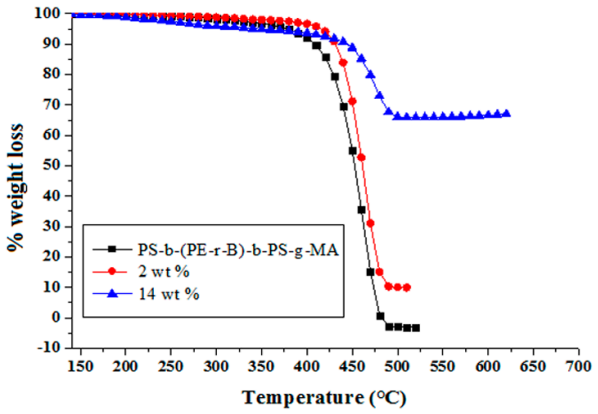

Figure 11. Thermogravimetric analysis (TGA) thermograms of neat PS-*b*-(PE-*r*-B)-*b*-PS-*g*-MA and composites with 2 wt % and 14 wt % Cu–Al_2O_3 loading.

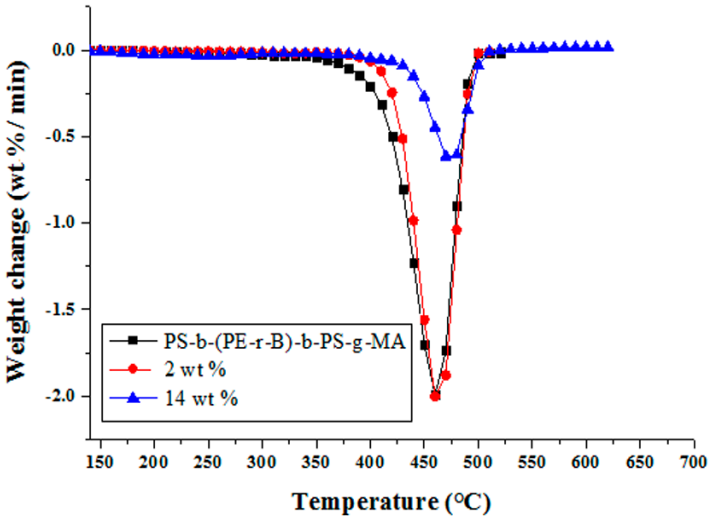

Figure 12. Derivative thermogravimetry (DTG) of neat PS-*b*-(PE-*r*-B)-*b*-PS-*g*-MA and composites with 2 wt % and 14 wt % Cu–Al_2O_3 loading.

3.6.2. Differential Scanning Calorimetry (DSC)

DSC analysis provides the determination of the glass transition temperature (T_g) of materials, the temperature at which a polymer transforms from a glassy to a rubbery state [60]. The DSC thermograms of neat PS-*b*-(PE-*r*-B)-*b*-PS-*g*-MA and the corresponding composites with 0, 2, and 14 wt % filler loading are shown in Figure 13. The stiffness of polymers is usually studied by T_g analysis. Stiff polymer chains with bulky, rigid side groups attached to the main chain imparts a high T_g. It is known that at T_g, polymer chains start to move. The results show that the incorporation of Cu–Al_2O_3 in the polymer matrix increases the T_g as the chains of PS-*b*-(PE-*r*-B)-*b*-PS-*g*-MA strongly adhere to the Cu–Al_2O_3 particles, which prevents free motion of polymer chains and hinders the segmental movement of chains [61,62].

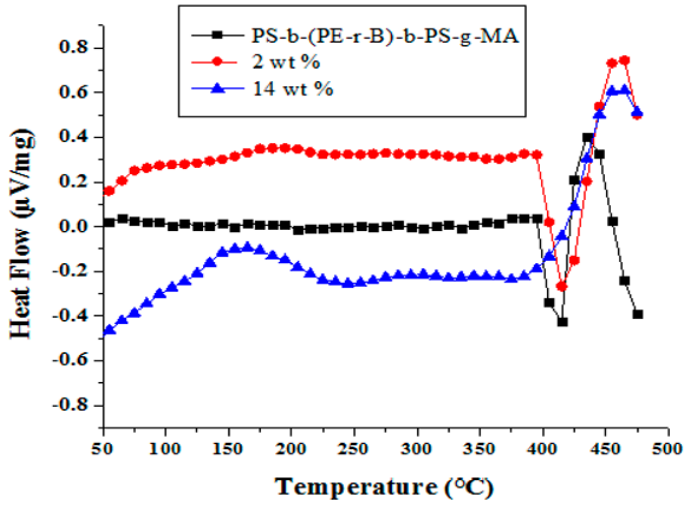

Figure 13. Differential scanning calorimetry (DSC) of neat PS-*b*-(PE-*r*-B)-*b*-PS-*g*-MA and composites with 2 wt % and 14 wt % Cu-Al_2O_3 loading.

4. Conclusions

In this study, nanocomposites were synthesized from the block copolymer polystyrene-*block*-poly(ethylene-*ran*-butylene)-*block*-polystyrene-graft-maleic anhydride (PS-*b*-(PE-*r*-B)-*b*-PS-*g*-MA) as

the matrix and from a filler material, prepared by the electroless deposition (ELD) of Cu particles on alumina powder. The nanocomposite belongs to the class of inorganic–organic composites containing metal-coated ceramic reinforcement agent embedded in a thermoplastic polymer insulation, categorized as conductive polymer nanocomposites. The nanocomposites are easy to prepare, show enhanced electrical conductivity, improved thermal stability, and mechanical properties. The pronounced increment in electrical conductivity with increased filler ratio, up to 7.692×10^{-5} S/cm in the case of 14 wt % filler loading, indicates the formation of conductive networks within the prepared composites. A good interfacial adhesion between filler and matrix permits to improve the Young's modulus and tensile strength at 14 wt % filler loading up to 159.475 MPa and 82.889 MPa, respectively. The composites also show improved thermal stability, while heat flow measurements via DSC show a higher glass transition temperature range with higher filler inclusion. XRD patterns indicate a more crystalline phase of the composites due to addition of metallic filler. SEM micrographs of the composites illustrate a uniform Cu deposition on Al_2O_3 and its homogeneous dispersion throughout polymer matrix when using the ELD technique. These results support the potential application of the prepared composites in electronic applications that require a prolonged shelf life, both in electronic semiconductors as in microelectronic packaging, EMI- and EDS-shielding materials, antistatic coatings for electronic, flexible IT devices, and others. Depending on the requirements of the applications, these materials may be used either in coatings or for standalone components.

Acknowledgments: Rohama Gill gratefully acknowledges the assistance of Muhammad Rafique (QAU) for mechanical analysis.

Author Contributions: Rohama Gill conceived and designed the experiments; QuratulAin Nadeem and Tasneem Fatima performed the experiments; Pepijn Prinsen and Rafael Luque analyzed the data; Aziz ur Rehman and Rashid Mahmood contributed reagents/materials/analysis tools; Rohama Gill, QuratulAin Nadeem and Tasneem Fatima wrote the paper.

Conflicts of Interest: The authors declare no conflict of interest.

References

1. Rimdusit, S.; Jubsilp, C.; Tiptipakorn, S. *Alloys and Composites of Polybenzoxazines: Properties and Applications*; Springer: Singapore, 2013; pp. 139–141.
2. Robinson, B.H. E-waste: An assessment of global production and environmental impacts. *Sci. Total Environ.* **2009**, *408*, 183–191. [CrossRef] [PubMed]
3. Shacham-Diamand, Y.; Osaka, T.; Okinaka, Y.; Sugiyama, A.; Dubin, V. 30 years of electroless plating for semiconductor and polymer micro-systems. *Microelectron. Eng.* **2015**, *132*, 35–45. [CrossRef]
4. Sudagar, J.; Lian, J.; Sha, W. Electroless nickel alloy composite and nano coatings—A critical review. *J. Alloys Compd.* **2013**, *571*, 183–204. [CrossRef]
5. Agarwala, R.C.; Agarwala, V. Electroless alloy composite coatings: A review. *Sadhana* **2003**, *28*, 475–493. [CrossRef]
6. Zhai, T.; Ding, C.; Lu, L.; Zhang, C. Autocatalytic deposition of copper coating on poly (ether ether ketone)/multiwalled carbon nanotubes composites via a palladium-free and simplified electroless process. *Mater. Lett.* **2015**, *147*, 46–49. [CrossRef]
7. Reddy, E.L.; Lee, H.C.; Kim, D.H. Steam reforming of methanol over structured catalysts prepared by electroless deposition of Cu and Zn on anodically oxidized alumina. *Int. J. Hydrogen Energy* **2015**, *40*, 2509–2517. [CrossRef]
8. Moon, J.H.; Kim, K.H.; Choi, H.W.; Lee, S.W.; Park, S.J. Electroless silver coating of rod-like glass particles. *Ultramicroscopy* **2008**, *108*, 1307–1310. [CrossRef] [PubMed]
9. Liu, S.; Liu, J.; Wang, L.; Zhao, F. Development of electrochemical DNA biosensor based on gold nanoparticle modified electrode by electroless deposition. *Bioelectrochemistry* **2010**, *79*, 37–42. [CrossRef] [PubMed]
10. Kretz, F.; Gacsi, Z.; Kovacs, J.; Pieczonka, T. The electroless deposition of nickel on SiC particles for aluminum matrix composites. *Surf. Coat. Technol.* **2004**, *180*, 575–579. [CrossRef]

11. Kuester, S.; Merlini, C.; Barra, G.M.; Ferreira, J.C.; Lucas, A.; de Souza, A.C.; Soares, B.G. Processing and characterization of conductive composites based on poly (styrene-b-ethylene-ran-butylene-b-styrene)(SEBS) and carbon additives: A comparative study of expanded graphite and carbon black. *Compos. Part B* **2016**, *84*, 236–247. [CrossRef]
12. Sarı, A.; Alkan, C.; Karaipekli, A.; Onal, A. Preparation, characterization and thermal properties of styrene maleic anhydride copolymer (SMA)/fatty acid composites as form stable phase change materials. *Energy Convers. Manag.* **2008**, *49*, 373–380. [CrossRef]
13. Araby, S.; Meng, Q.; Zhang, L.; Kang, H.; Majewski, P.; Tang, Y. Electrically and thermally conductive elastomer/graphene nanocomposites by solution mixing. *J. Polym.* **2014**, *55*, 201–210. [CrossRef]
14. Tian, Q.H.; Guo, X.Y. Simulation of electromagnetic-flow fields in Mg melt under pulsed magnetic field. *Trans. Nonferrous Met. Soc. China* **2010**, *20*, 283–287. [CrossRef]
15. *Standard Test Methods for DC Resistance or Conductance of Insulating Materials*; ASTM D257-07; ASTM International: West Conshohocken, PA, USA, 2007.
16. *Standard Test Method for Tensile Properties of Plastics*; ASTM D638-02; ASTM International: West Conshohocken, PA, USA, 2002.
17. *Standard Test Method for Tensile Properties of Plastics*; ASTM D638-03; ASTM International: West Conshohocken, PA, USA, 2003.
18. Ma, H.; Liu, Z.; Wu, L.; Wang, Y.; Wang, X. Study of a pre-treatment process for electroless copper plating on ceramics. *Thin Solid Films* **2011**, *519*, 7860–7863. [CrossRef]
19. Mondin, G.; Lohe, M.R.; Wisser, F.M.; Grothe, J.; Mohamed-Noriega, N.; Leifert, A.; Dorfler, S.; Bachmatiuk, A.; Rummelib, M.H.; Kaskel, S. Electroless copper deposition on (3-mercaptopropyl) triethoxysilane-coated silica and alumina nanoparticles. *Electrochim. Acta* **2013**, *114*, 521–526. [CrossRef]
20. Reddy, K.R.; Sin, B.C.; Yoo, C.H.; Park, W.; Ryu, K.S.; Lee, J.S.; Shon, D.; Lee, Y. A new one-step synthesis method for coating multi-walled carbon nanotubes with cuprous oxide nanoparticles. *Scr. Mater.* **2008**, *58*, 1010–1013. [CrossRef]
21. Chang, H.F.; Saleque, M.A.; Hsu, W.S.; Lin, W.H. Characterization and dehydrogenation activity of $CuAl_2O_3$ catalysts prepared by electroless plating technique. *J. Mol. Catal. A Chem.* **1996**, *109*, 249–260. [CrossRef]
22. Sharma, R.; Agarwala, R.C.; Agarwala, V. Development of copper coatings on ceramic powder by electroless technique. *Appl. Surf. Sci.* **2006**, *252*, 8487–8493. [CrossRef]
23. Leon, C.A.; Rodriguez-Ortiz, G.; Nanko, M.; Aguilar, E.A. Pulsed electric current sintering of Cu matrix composites reinforced with plain and coated alumina powders. *Powder Technol.* **2014**, *252*, 1–7. [CrossRef]
24. Silvain, J.F.; Bobet, J.L.; Heintz, J.M. Electroless deposition of copper onto alumina sub-micronic powders and sintering. *Compos. Part A Appl. Sci. Manuf.* **2002**, *33*, 1387–1390. [CrossRef]
25. Wang, H.; Jia, J.; Song, H.; Hu, X.; Sun, H.; Yang, D. The preparation of Cu-coated Al_2O_3 composite powders by electroless plating. *Ceram. Int.* **2011**, *37*, 2181–2184. [CrossRef]
26. Krupa, I.; Miková, G.; Novák, I.; Janigová, I.; Nógellova, Z.; Lednický, F.; Prokes, J. Electrically conductive composites of polyethylene filled with polyamide particles coated with silver. *Eur. Polym. J.* **2007**, *43*, 2401–2413. [CrossRef]
27. Goyal, R.K.; Tiwari, A.N.; Mulik, U.P.; Negi, Y.S. Novel high performance Al_2O_3/poly (ether ether ketone) nanocomposites for electronics applications. *Compos. Sci. Technol.* **2007**, *67*, 1802–1812. [CrossRef]
28. Choi, S.; Kim, K.; Nam, J.; Shim, S.E. Synthesis of silica-coated graphite by enolization of polyvinylpyrrolidone and its thermal and electrical conductivity in polymer composites. *Carbon* **2013**, *60*, 254–265. [CrossRef]
29. Al-Saleh, M.H.; Saadeh, W.H.; Sundararaj, U. EMI shielding effectiveness of carbon based nanostructured polymeric materials: A comparative study. *Carbon* **2013**, *60*, 146–156. [CrossRef]
30. Chu, B.; Zhou, X.; Ren, K.; Neese, B.; Lin, M.; Wang, Q.; Bauer, F.; Zhang, Q.M. A dielectric polymer with high electric energy density and fast discharge speed. *Science* **2006**, *313*, 334–336. [CrossRef] [PubMed]
31. Rahaman, M.; Chaki, T.K.; Khastgir, D. Development of high performance EMI shielding material from EVA, NBR, and their blends: effect of carbon black structure. *J. Mater. Sci.* **2011**, *46*, 3989–3999. [CrossRef]
32. Dang, Z.M.; Yuan, J.K.; Zha, J.W.; Zhou, T.; Li, S.T.; Hu, G.H. Fundamentals, processes and applications of high-permittivity polymer–matrix composites. *Prog. Mater. Sci.* **2012**, *57*, 660–723. [CrossRef]

33. Xu, S.; Rezvanian, O.; Peters, K.; Zikry, M.A. The viability and limitations of percolation theory in modeling the electrical behavior of carbon nanotube–polymer composites. *Nanotechnology* **2013**, *24*, 155706. [CrossRef] [PubMed]
34. Pang, H.; Xu, L.; Yan, D.X.; Li, Z.M. Conductive polymer composites with segregated structures. *Prog. Polym. Sci.* **2014**, *39*, 1908–1933. [CrossRef]
35. Deng, H.; Lin, L.; Ji, M.; Zhang, S.; Yang, M.; Fu, Q. Progress on the morphological control of conductive network in conductive polymer composites and the use as electroactive multifunctional materials. *Prog. Polym. Sci.* **2014**, *39*, 627–655. [CrossRef]
36. Hu, J.; Zhang, H.B.; Hong, S.; Jiang, Z.G.; Gui, C.; Li, X.; Yu, Z.Z. Simultaneous improvement in both electrical conductivity and toughness of polyamide 6 nanocomposites filled with elastomer and carbon black particles. *Ind. Eng. Chem. Res.* **2014**, *53*, 2270–2276. [CrossRef]
37. Arjmand, M.; Mahmoodi, M.; Gelves, G.A.; Park, S.; Sundararaj, U. Electrical and electromagnetic interference shielding properties of flow-induced oriented carbon nanotubes in polycarbonate. *Carbon* **2011**, *49*, 3430–3440. [CrossRef]
38. Zheng, W.; Wong, S.C. Electrical conductivity and dielectric properties of PMMA/expanded graphite composites. *Compos. Sci. Technol.* **2003**, *63*, 225–235. [CrossRef]
39. Wei, Y.F.; Li, Z.Q. Measurement of specific contact resistivity using scanning voltage probes. *Appl. Phys. Lett.* **2013**, *102*, 131605.
40. Al-Saleh, M.H. Influence of conductive network structure on the EMI shielding and electrical percolation of carbon nanotube/polymer nanocomposites. *Synth. Met.* **2015**, *205*, 78–84. [CrossRef]
41. Nadeem, Q.; Rizwan, M.; Gill, R.; Rafique, M.; Shahid, M. Fabrication of alumina based electrically conductive polymer composites. *J. Appl. Polym. Sci.* **2016**, *133*. [CrossRef]
42. Choi, S.H.; Kim, D.H.; Raghu, A.V.; Reddy, K.R.; Lee, H.I.; Yoon, K.S.; Jeong, H.M.; Kim, B.K. Properties of graphene/waterborne polyurethane nanocomposites cast from colloidal dispersion mixtures. *J. Macromol. Sci. Part B Phys.* **2012**, *51*, 197–207. [CrossRef]
43. Sau, K. Acetylene black filled Elastomeric conductive composites based on EPDM, NBR and Silicone rubber. *History* **2015**, *15*, 13–19.
44. Sohi, N.J.S.; Rahaman, M.; Khastgir, D. Dielectric property and electromagnetic interference shielding effectiveness of ethylene vinyl acetate-based conductive composites: Effect of different type of carbon fillers. *Polym. Compos.* **2011**, *32*, 1148–1154. [CrossRef]
45. Verma, P.; Saini, P.; Malik, R.S.; Choudhary, V. Excellent electromagnetic interference shielding and mechanical properties of high loading carbon-nanotubes/polymer composites designed using melt recirculation equipped twin-screw extruder. *Carbon* **2015**, *89*, 308–317. [CrossRef]
46. Kwon, S.C.; Adachi, T.; Araki, W.; Yamaji, A. Effect of composing particles of two sizes on mechanical properties of spherical silica-particulate-reinforced epoxy composites. *Compos. Part B Eng.* **2008**, *39*, 740–746. [CrossRef]
47. Fletcher, A.; Gupta, M.C. Mechanical properties of elastomer nanocomposites for electromagnetic interference shielding applications. *J. Compos. Mater.* **2014**, *48*, 1261–1276. [CrossRef]
48. Bishay, I.K.; Abd-El-Messieh, S.L.; Mansour, S.H. Electrical, mechanical and thermal properties of polyvinyl chloride composites filled with aluminum powder. *Mater. Des.* **2011**, *32*, 62–68. [CrossRef]
49. Gao, H.; Ji, B.; Jäger, I.L.; Arzt, E.; Fratzl, P. Materials become insensitive to flaws at nanoscale: Lessons from nature. *Proc. Natl. Acad. Sci. USA* **2003**, *100*, 5597–5600. [CrossRef] [PubMed]
50. Tang, L.S.; Mariatti, M. Comparison on the properties of nickel-coated graphite (NCG) and graphite particles as conductive fillers in polypropylene (PP) composites. *Polym. Plast. Technol. Eng.* **2009**, *48*, 614–620. [CrossRef]
51. Kuo, M.C.; Tsai, C.M.; Huang, J.C.; Chen, M. PEEK composites reinforced by nano-sized SiO_2 and Al_2O_3 particulates. *Mater. Chem. Phys.* **2005**, *90*, 185–195. [CrossRef]
52. Chen, Y.; Zhou, S.; Yang, H.; Wu, L. Structure and properties of polyurethane/nanosilica composites. *J. Appl. Polym. Sci.* **2005**, *95*, 1032–1039. [CrossRef]
53. Renner, K.; Yang, M.S.; Móczó, J.; Choi, H.J.; Pukánszky, B. Analysis of the debonding process in polypropylene model composites. *Eur. Polym. J.* **2005**, *41*, 2520–2529. [CrossRef]
54. Wang, K.; Wu, J.; Ye, L.; Zeng, H. Mechanical properties and toughening mechanisms of polypropylene/barium sulfate composites. *Compos. Part A Appl. Sci. Manuf.* **2003**, *34*, 1199–1205. [CrossRef]

55. Zhang, Q.; Tian, M.; Wu, Y.; Lin, G.; Zhang, L. Effect of particle size on the properties of $Mg(OH)_2$-filled rubber composites. *J. Appl. Polym. Sci.* **2004**, *94*, 2341–2346. [CrossRef]
56. Ku, H.; Wang, H.; Pattarachaiyakoop, N.; Trada, M. A review on the tensile properties of natural fiber reinforced polymer composites. *Compos. Part B Eng.* **2011**, *42*, 856–873. [CrossRef]
57. Zhou, W.; Qi, S.; Li, H.; Shao, S. Study on insulating thermal conductive BN/HDPE composites. *Thermochim. Acta* **2007**, *452*, 36–42. [CrossRef]
58. Meincke, O.; Kaempfer, D.; Weickmann, H.; Friedrich, C.; Vathauer, M.; Warth, H. Mechanical properties and electrical conductivity of carbon-nanotube filled polyamide-6 and its blends with acrylonitrile/butadiene/styrene. *Polymer* **2004**, *45*, 739–748. [CrossRef]
59. Shafiq, M.; Yasin, T.; Saeed, S. Synthesis and characterization of linear low-density polyethylene/sepiolite nanocomposites. *J. Appl. Polym. Sci.* **2012**, *123*, 1718–1723. [CrossRef]
60. Vilaplana, F.; Ribes-Greus, A.; Karlsson, S. Analytical strategies for the quality assessment of recycled high-impact polystyrene: A combination of thermal analysis, vibrational spectroscopy, and chromatography. *Anal. Chim. Acta* **2007**, *604*, 18–28. [CrossRef] [PubMed]
61. Lee, J.G.; Kim, S.H.; Kang, H.C.; Park, S.H. Effect of TiO_2 on PVDF/PMMA composite films prepared by thermal casting. *Macromol. Res.* **2013**, *21*, 349–355. [CrossRef]
62. Xie, S.H.; Zhu, B.K.; Wei, X.Z.; Xu, Z.K.; Xu, Y.Y. Polyimide/$BaTiO_3$ composites with controllable dielectric properties. *Compos. Part A Appl. Sci. Manuf.* **2005**, *36*, 1152–1157. [CrossRef]